PHYSICAL REVIEW MATERIALS **7**, 083402 (2023)

Two-dimensional phase field crystal simulation of laser-induced recrystallization: A mechanism of grain-boundary phonon scattering and softening

Duncan Burns,[*] Nikolas Provatas, and Martin Grant
Department of Physics, McGill University, Montréal, Québec, Canada H3A 2T8

(Received 13 May 2023; accepted 18 July 2023; published 14 August 2023)

In this article we present, as far as we know, the first numerical investigation of phonon relaxation in two-dimensional polycrystalline systems simulated with a multitimescale phase field crystal model. We first measure the phonon spectrum averaged over different polycrystalline configurations using thermal fluctuations to capture the rapid processes. We find two main peaks in the spectrum attributable, respectively, to dampening and softening of different wavelength phonons. In particular, it is shown that polycrystals have a phonon caging regime, a signature of amorphous materials. Subsequently, we report on a mechanism of grain-boundary melting resulting from the accumulation of phonon scattering. We find this behavior exhibited in both rapid temperature annealing of polycrystalline samples and from input of kinetic energy representative of rapid laser heating or hot-rolling. In the latter case, we theorize a rate relation between the maximally achieved liquid fraction as a function of the initial kinetic energy, defining a metastable activation energy that can be measured in experiments. We expect that the scattering mechanisms investigated in this work underpin grain-boundary melting and recrystallization processes encountered in rapid solidification experiments.

DOI: 10.1103/PhysRevMaterials.7.083402

I. INTRODUCTION

Despite significant progress in understanding how the microstructure controls the properties of many materials, the dynamical mechanisms that govern nonequilibrium microstructure formation remain arcane. The challenge is tied to the plethora of interaction pathways between competing time- and length scales. In this sense, the behavior of a metal is subject to the underlying atomic lattice structure that sets a fundamental length scale. Depending on local available energy, the atoms can break their spatial symmetry to form a melt, void, fracture, or nucleate a dislocation. These metastable defect structures are linked to resultant changes in macroscale properties, such as hardness or ductility. In addition to the length scale, vibration of atoms sets a fundamental timescale. Phonons propagate through a material, transferring energy that can precipitate defects, cause phase transformations, or recrystallization. The scattering of phonons off metastable structures can also alter the transport properties, such as thermal conductivity. To fabricate optimized materials in rapid processes such as additive manufacturing or shock peening, the study of dynamical defect formation and plasticity is ergo imperative.

The preferential recrystallization at sites of high strain energy is well documented [1]. This idea is crucial in rolling, where polycrystals are mechanically distorted [2]. Recent experiments on stainless steels [3,4] have demonstrated that energy input from a laser, or shock front [5], can have a similar effect. With lower imparted energies, long-lived melt pools have been found that emanate from grain boundaries [6,7]. Liquid close to the solidification temperature has been measured with incoherent neutron scattering to capture the caging regime of the dynamic structure factor [8], a feature that has been recently reported in polycrystals [9]. Unfortunately, some of these experiments rely on postmortem analyses. As a result, the dynamical mechanisms at play remains elusive.

During material processing, phonons scatter and soften, potentially increasing the local energy density through dampening. Many studies have been conducted on the thermal transport behavior in amorphous materials, where the lack of long-range structure allows excessive phonon dampening [10,11]. The energy absorption can be seen by frequency peaks in the phonon density of states, amenable to Raman scattering experiments. Meanwhile, dips in spectrum denote regions of phonon depletion. A large band is often found in the terahertz frequency range, termed the boson peak. In recent literature, conflicting arguments have been given of the cause of the boson peak [12–14]. Starting from a dampening process in the dispersion relation, Bagglioli *et al.* demonstrated the appearance of such a peak feature [15,16]. Often associated to glassy materials, polycrystals have been shown to exhibit similar caging properties as in glasses [9]. We thus expect that polycrystals also exhibit a boson peak with suppressed prominence, depending on the grain-boundary density. At lower frequencies, Van Hove singularities can also appear in polycrystalline materials, whose dispersion relation becomes singular. Herein we show the existence of both types of peak structures and their contributions from phonons of different length scales.

Few simulation methods exist to complement experiments in the study the late stage diffusion behavior resulting from phononic propagation. Conventional phonon scattering

---

[*] Author to whom correspondence should be addressed: duncan.burns@mail.mcgill.ca

analyses at the atomistic scale can be carried out with molecular dynamics. However, phonon coupling to the resultant structure profile can be intractable to explore due to the limiting numerical time step by vacancy hopping. For this reason, we employ the phase field crystal (PFC) methodology originally developed Elder *et al.*, which simulates the temporally averaged density field [17] of a material. Phase field crystal methods have been systematically advanced since the early 2000s and have already demonstrated their effectiveness for investigating solidification of different crystal structures [18–21] and topological plasticity in the solid state [22–26]. Although originally describing only diffusive growth, recent progress has extended the hydrodynamic framework of the PFC methodology to examine phonon scattering on subdiffusive timescales but still longer than MD timescales [27–29]. These multitimescale models are often said to propagate *quasiphonons*.

This article shows the results of a novel study on phonon-triggered recrystallization in two spatial dimensions. First, we provide a brief overview of the phase field crystal (PFC) model and our simulation approach. Subsequently, we illustrate three novel procedures in the context of PFC simulations that allow measurements of the intermediate scattering function, longitudinal density of states, and an approximation of the input kinetic energy. We then detail new results on the appearance of a boson peak and secondary grain-boundary Van Hove singularity in polycrystaline materials. Finally, we study the input of kinetic energy into polycrystalline samples, thus triggering melting and crystallization. We propose a potential rate relation that describes the maximally achieved metastable defect-fraction (e.g., melt pools, dislocations, etc.) as a function of the input kinetic energy. We expect that the resultant mechanism explored herein are of frequent occurrence in rapid solidification processing, including in additive manufacturing, and may help elucidate current challenges with these emerging methods.

II. INVESTIGATION OF POLYCRYSTALLINE PHONON SCATTERING

A. Model

Phase field crystal models hearken back to the work of Elder *et al.* [17]. Here the authors construct a pseudo–Landau-Ginzburg theory for a time-averaged density field, which implicitly subsumes contributions from thermal and phonon vibrations. The model has been demonstrated to describe dynamic plasticity on the atomic scale, both qualitatively [18,22] and quantitatively [24,30]. The inherent anisotropy further permits studies of interface driven diffusion [31] and grain-boundary premelting. The technique has also exhibited glassy behaviors [23,32,33], to which we shall later make connections.

The model begins by construction of an effective free energy, F, as a functional of the density field, ρ. Expanding about a uniform reference density near the transition point, ρ_{ref}, the free energy can be split into ideal gas and interaction components [34], the latter of which takes the form of a series of correlations of increasing order. Expanding the ideal contribution near the reference density, and keeping only contributions from the two-point correlation results in Ref. [35],

$$\frac{F}{\rho_{\mathrm{ref}} k_b T} = \int_{\Omega} \left[\frac{\rho^2}{2} - \frac{\rho^3}{6} + \frac{\rho^4}{12} - \frac{\rho^2}{2}(1 - B_l) + \rho B_x \left(R^2 \nabla^2 \rho + \frac{R^4}{2} \nabla^4 \rho \right) \right], \qquad (1)$$

where the free energy has been recast into dimensionless units by division through the Boltzmann energy scale $k_b T$ and the reference density. Here Ω refers to the simulation domain. B_x, B_l, and R, are components of the assumed two-point correlation function, while B_l controls the liquid compressibility and has some intrinsic temperature dependence. Meanwhile, B_x controls the solid pressure and compressibility and has an inherent temperature dependence as described in Appendix A. Below a certain temperature, the correlation causes the hexagonal phase of atomic length R to be a minimum energy configuration, while at higher temperatures the systems favors the formation of a uniform density distribution. Appendix A describes the thermodynamic phase diagram of the model for liquid-solid coexistence. It is also noted that modifications of the two-point correlation and inclusion of higher-order correlations can allow for further crystallographic phases or vapor phases [36,37]. Additional fields can also be added to allow for description of multicomponent alloys [20].

The dynamics of the phase field crystal density field propagate through a damped wavelike equation derived in detail in our earlier work [29]. This is given by

$$\frac{\partial^2 \rho}{\partial t^2} + \beta_0 \frac{\partial \rho}{\partial t} - \beta_2 \nabla^2 \left(\frac{\partial \rho}{\partial t} \right) = D \nabla^2 \left(\frac{\delta F}{\delta \rho} \right) + \nabla \cdot \eta, \qquad (2)$$

where gradients in the chemical potential, $\mu = \frac{\delta F}{\delta \rho}$, act as a source of both diffusive and wavelike density propagation in a solid. The mobility parameter, D, is assumed constant here, though some thermal and dynamic dependencies may already be embedded in the form of the free energy attained after coarse-graining in time. The vector field η denotes a noise current representative of fast processes on the order the atomic vibrations and which have been averaged out in the free-energy functional. The noise current is assumed to obey, $\langle \eta_i \rangle = 0$ and $\langle \eta_i \eta_j \rangle = \sigma \delta_{ij}$, where δ_{ij} is the Kronecker delta between vector directions i and j. This relation is in accordance with the fluctuation-dissipation theorem where σ is on order of the thermal scale. As argued in our previous work [29], dissipation arising from vacancy diffusion is attributable to the β_0 term. Meanwhile, as far as we know, the β_2 term is a novel addition to previous PFC works with phonon effects [27,28], affecting the dissipation based on the wavevector modes of the signal, thus allowing for a description of phonon softening. The parameter β_2 may also be viewed as a phase-dependent modulation to the dissipation. The additional dampening arises from temperature and phonon-phonon scattering that are evidently important for our current work. When the dissipation approaches infinity, the wave model reduces to the conventional local diffusive model. The inclusion of the first, inertial, term provides a short timescale that is important for rapid elastic relaxation in dynamics, a feature that can significantly change dislocation dynamics and the

TABLE I. List of parameters used during this investigation. L denotes the length of the square numeric grid. Qualitative units are reported, which favor the hexagonal solid phase. The numerical spacings dx and dy were chosen such that the atomic spacing $a_o \approx 10dx$.

$\rho_{\text{ref}}k_bT$	B_l	B_x	R	β_0	β_2	D	dt	dx	dy	L
1	1.0	0.98	1	0.1	$0.1 \rightarrow 1$	1	0.01	0.8502	0.9817	512

growth morphology a solid-liquid front (e.g., from planar to cellular). It is noteworthy that the full model of Ref. [29] also included strain diffusion, which was argued to modify dislocation climb and glide timescale. This effect was also recently introduced effectively into an PFC amplitude model framework [38].

For simulations reported in this work we use the set of model parameters listed in Table I, which also includes the numerical parameters used. We solve Eq. (2) through the pseudospectral method that was developed previously [29].

B. Polycrystalline sample construction

We studied phonon scattering in polycrystalline samples solidified in the phase space of the aforementioned PFC model. The construction of a polycrystalline material whose grain-boundary distribution matches experiments can be quite challenging. In selective laser melting, grain structures resemble those achieved in directional solidification experiments. Depending on the rapidity of the process, grains may develop as cellular fronts or dendritic networks that impinge. In the former scenario when the characteristics Mullins-Sekerka wavelength is large, grain sizes can be thousands of atoms large. The plasticity of such configurations is believed to be dominated by lone dislocations and geometrically necessary dislocations near cell boundaries. Meanwhile, the grain structure of crystals comprising impinged dendritic networks can be composed of many smaller high-angle nanograin boundaries. Nanocrystalline structure is generally accompanied by vacancy clusters [39], whose local thermodynamics may favor fracture or melt-pool formation. On recrystallization these metastable defects may cause large misorientation gradients [40]. We further note that unstable growth below the spinodal can also generate a plethora of metastable structures. It is noted that it is often difficult to gather ample statistics of such structures from experiments. Furthermore, the nonequilibrium extent of such structures can be challenging to ascertain.

In this work, we focus on reproducing a realistic statistical distribution of grains, with an emphasis on different misorientation grain boundaries. We constructed 50 simulation samples that were initialized with normally distributed angles and random initial seed sizes and number. To allow for crystallization, the seeds were placed inside an undercooled liquid melt, and the system was then allowed to grow according to Eq. (2) until grain impingement. An illustration of a typical polycrystalline sample during the growth phase is shown in Fig. 1(a). The impingement criterion can be found by observing changes in the slope of the free energy in time. An example of one of our fully solidified polycrystalline samples is shown in Fig. 1(b), where a strain map is provided to highlight the dipolar character of individual dislocations that emerge after impingement. Lines of jammed dislocations separate the individual grains from another. We note that some long-range strains are found within bulks that result from the bending of slip lines. Our typical grain sizes range between 4 to 50 atoms in length. The resultant grains can subsequently

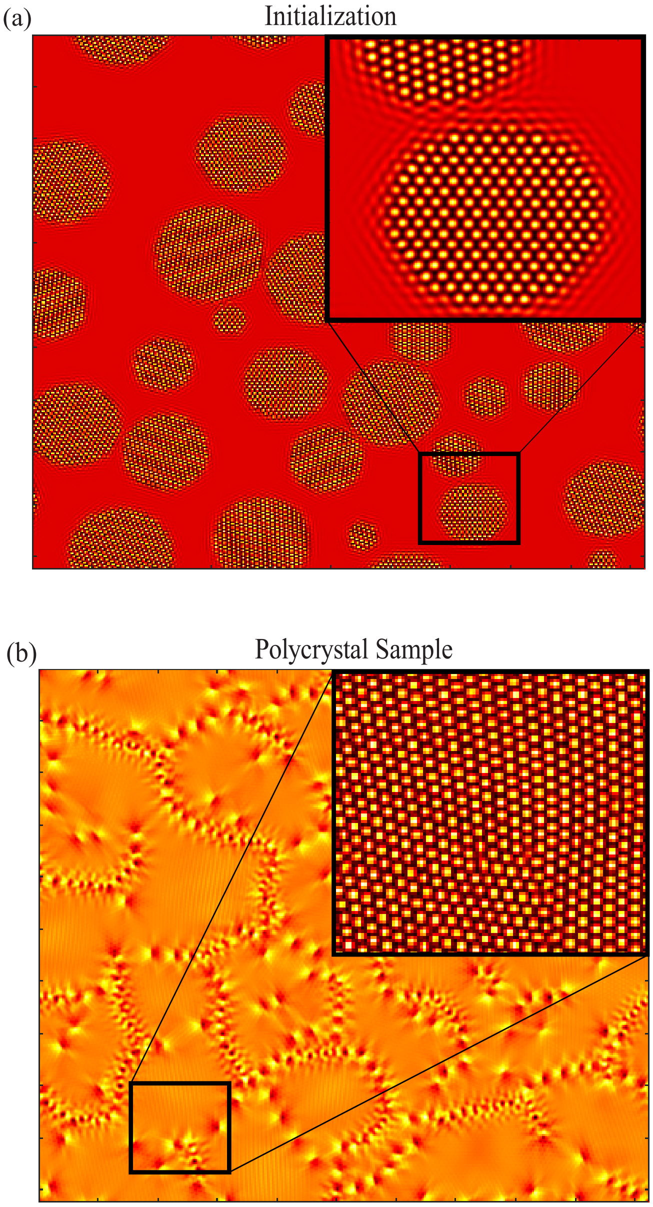

FIG. 1. Illustration of the phase field crystal density field during polycrystalline growth on a 1024^2 simulation domain. Panel (a) highlights the structure after 100 time steps with an initial distribution of circular seeds. After 5000 time steps, the uniform liquid phase almost fully crystallizes and individual grains impinge on each other. (b) The resultant hydrostatic strain map of the impinged polycrystal, which uses the density filter introduced in Appendix A. The inset magnifies the density field of a grain-boundary region.

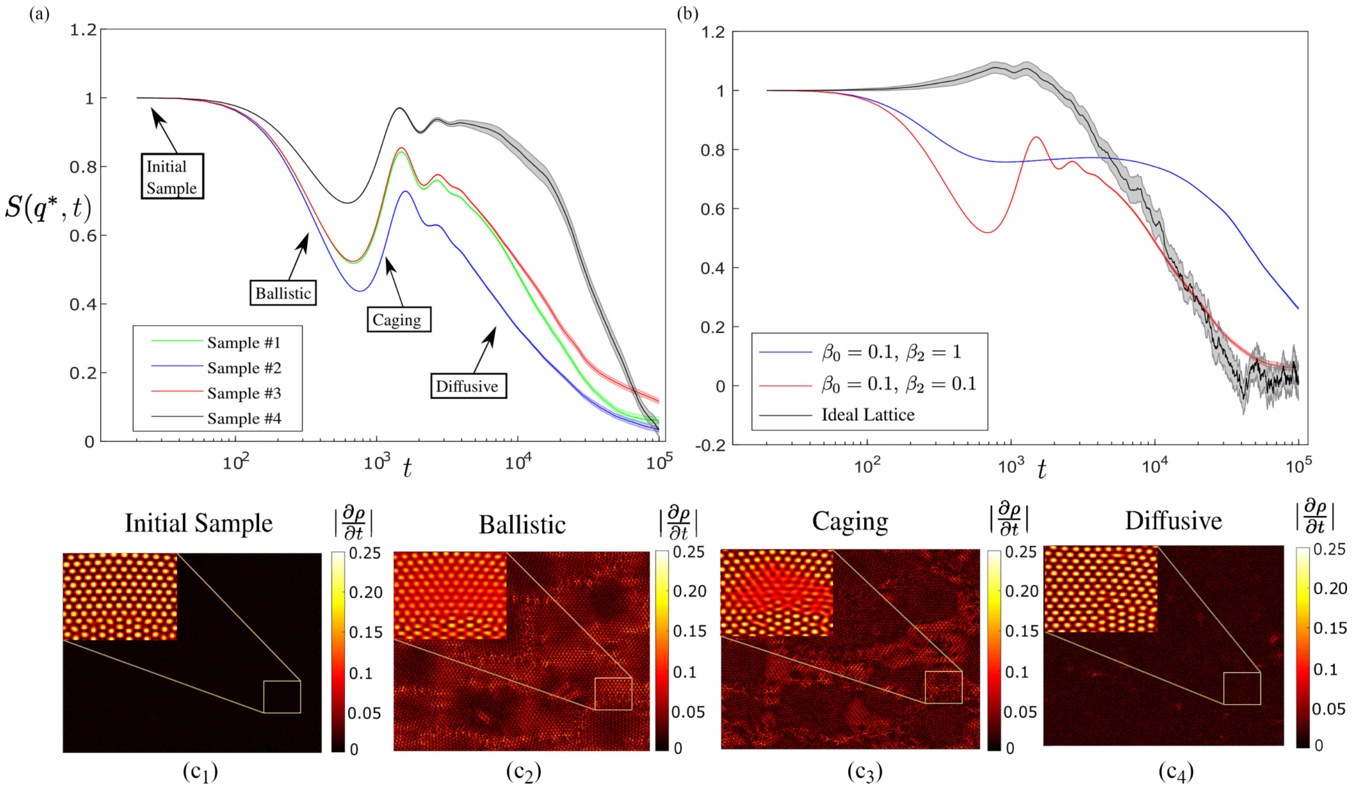

(c$_1$) (c$_2$) (c$_3$) (c$_4$)

FIG. 2. Illustrated is the dynamic structure factor, $S(q^*, t)$, measured at the reciprocal lattice wave vector q^*, as a function of time, t. Panel (a) shows a comparison of $S(q^*, t)$ for four polycrystalline samples with different initial grain size distributions. The curves are supplemented with a transparent bordered region denoting the standard error attained from averaging over 10 different realizations of thermal noise ($\sigma = 0.2$). Panel (b) depicts the dependence of $S(q^*, t)$ with different model dissipation values. The decay behavior of an ideal crystal is also illustrated in gray. The maps of $|\frac{\partial\rho}{\partial t}|$ highlight the dynamic behavior of samples at differing stages of evolution: initial sample, ballistic regime, β dissipation (caging) regime, and α dissipation (diffusive) regime, respectively. An inset is provided in each map that highlights a subsection of the density field, which was grain boundary in the initial impinged sample.

be characterized through their grain number, grain size, strain distribution ($\langle\nabla \cdot u^2\rangle$), and energy distribution.

C. Intermediate scattering function

A metric often used in incoherent neutron scattering of polycrystalline materials is the self-intermediate scattering function, or dynamic structure factor, $S(q, t)$. This can be evaluated by

$$S(q, t) = \langle\tilde{\rho}_{-q,0}\tilde{\rho}_{q,t}\rangle, \tag{3}$$

where $\tilde{\rho}_{q,t}$ denotes the Fourier transform of the density field at wave-vector magnitude q and time t. The average, $\langle\cdot\rangle$, is performed over realizations of the thermal noise and all radial variations of wave vectors of magnitude (q). To compare with experimental results, one would further average over crystalline configurations, though the main features are expected to be self-averaging over large-enough samples.

The structure factor provides information about the nature of the crystal evolution. Berry *et al.* have previously used this metric in binary phase field crystal models to illustrate caging in glassy undercooled melts [30] where a timescale competition exists between different atomic species. In such cases, the intermediate scattering function exhibits multistage stretched exponential relations, with additional stages resulting from the timescale of heterogeneous escape. We have found similar evidence in relation to the competition of mass and phonon motions in polycrystalline samples, as will be shown below. Namely, phonon caging results in an extension of a plateau region between the ballistic and diffusive dynamic regimes, which is often termed β relaxation in neutron scattering experiments of glassy materials. Molecular dynamics studies conducted by Zhang *et al.* originally showed that polycrystals may share this glasslike feature [9]. We note that a dip prior to the β-relaxation regime has been referred to in the studies of glasses to be related to the so-called boson peak [41]. In the context of polycrystalline materials, the extent of the plateau may shed some light on the inherent amorphous structure of grain boundaries and defects.

Thus we measured $S(q, t)$ for the evolution of the polycrystals that we created earlier. The evolution was simulated in the presence of a large noise, $\sigma = 0.2$. This choice of noise amplitude was chosen to represent the highly nonequilibrium excitation strains that develop in a material during a large ad hoc quench. The measured $S(q, t)$ is illustrated in Fig. 2(a) for a number of polycrystalline samples exhibiting similar two-timescale behavior. The crossover behavior between the ballistic and caging regimes was found to be impacted by the amount of high wave-vector dissipation, which is controlled through β_2. This is illustrated in Fig. 2(b) of the same figure, which also includes the structure function evolution of an idealized lattice that only contains a single decay timescale.

Figures 2(c$_1$)–2(c$_4$) illustrate $|\frac{\partial\rho}{\partial t}|$ at different stages of the structure evolution. Here an initial seed (c$_1$) begins inactivated, subsequently releasing elastic propagations that diffuse (c$_2$). This *quasiphonon* diffusion takes the density configuration away from the starting state. Although no plastic deformation is associated with this early response, the time averaged density field varies in local amplitude. The ballistic diffusion factor may then be deduced from the initial exponential decay scale seen in Fig. 2(a). In an idealized lattice only local amplitude fluctuations drive the system out of the starting configuration as was observed in Fig. 2(b). In polycrystalline materials however, a significant portion of kinetic energy and activity is limited (caged) near to the grain boundaries, while grain bulks remain relatively unchanged. This behavior is observed in Fig. 2(c$_3$) and constitutes the crossover regime between *quasiphonon* diffusion and plastic diffusion. As *quasiphonons* are depleted from the grain bulks, large density regions remain unperturbed. As a result the autocorrelation function plateaus. Meanwhile, phonons scatter off and collect at sites of high energy. This allows for the formation of metastable states. In multicomponent alloys, intermetallic phases may form. In our pure material system, recrystallization follows and the system grows and coarsens through mass diffusion [Fig. 2(c$_4$)]. Rough estimates of required annealing times can be garnered from analyzing the decay scale of the dynamic structure factor.

D. Longitudinal phonon density of states

The rapid imparting of laser energy into a lattice can cause temperature pile-up, a property of phonon scattering and softening that contributes to the caging-regime described above. This necessitates the investigation of the spectrum of phonon frequencies and energies, which can be analyzed through the phonon density of states, $\mathcal{G}(\omega)$. Following molecular hydrodynamics [42], the density of states can be calculated through

$$\mathcal{G}(\omega) = \mathcal{F}_\omega\left[N\int_\Omega d^2q\langle \vec{g}(q,0)\cdot\vec{g}(q,t)\rangle S(q,t)\right], \qquad (4)$$

where N is a normalization constant, $\vec{g}(q,t)$ is the Fourier transform of the local momentum density, and $\langle\cdot\rangle$ is a thermal average as performed in the calculation of the intermediate scattering function $S(q,t)$. This metric is often probed in Raman spectroscopy to understand which phonons frequencies are the active energy carriers in a given process. In such studies the longitudinal and transverse momentum contributions can be separated through use of the incident polarization. The phonon density of states has remained a valuable metric in thermal conductivity optimization. Moreover, the phonon density of states can differentiate between glassy structures and pristine lattices, the reason for which is that glassy materials exhibit additional scattering and dampening, hence resulting in harmonic sets of peaks in the vibrational spectrum.

Even a qualitative assessment of the phonon density of states has remained elusive in phase field crystal modeling, as the momentum has not been extractable. This has made the study of phonon behaviours challenging to compare to experiments. However, by making use of the Helmholtz decomposition a relation between the longitudinal momentum, $\vec{g}_l$, and $\frac{\partial\rho}{\partial t}$ can be developed. Since hydrodynamics constitutes the basis for the derivation of our dynamical model, we exploit the mass continuity equation, writing it as

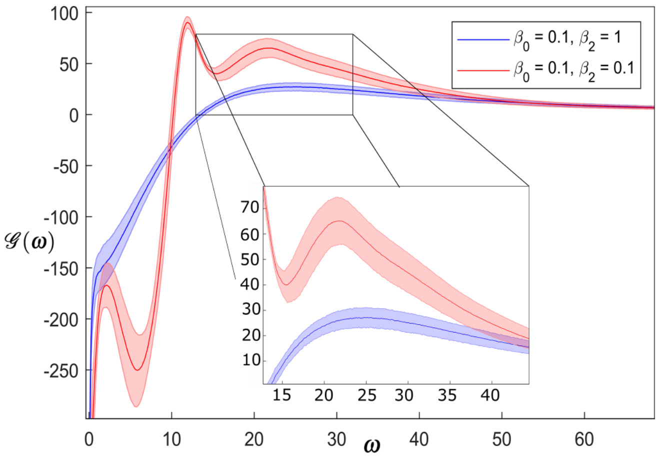

FIG. 3. Normalized longitudinal phonon density of states for two values of β_2 dissipation. The inset focuses on the high-frequency broad peak exhibited by both data sets. The frequency, ω, is given in units of the inverse of the time step, dt^{-1}. As we have alluded to earlier, the negative density of states should be interpreted as a depletion of longitudinal modes. The transparent borders reflect the standard error of the measured averaged of polycrystal samples.

$$\frac{\partial\rho}{\partial t} = \nabla\cdot\vec{g} = \nabla\cdot(\nabla\phi_{\vec{g}} + \nabla\times H_{\vec{g}}) = \nabla^2\phi_{\vec{g}}. \qquad (5)$$

Here the momentum has been decomposed into longitudinal, $\vec{g}_l = \nabla\phi_{\vec{g}}$, and shear, $\vec{g}_s = \nabla\times H_{\vec{g}}$, modes. Taking the derivatives to Fourier space then permits a relation between the longitudinal component and $\frac{\partial\rho}{\partial t}$ given by

$$\vec{g}_l = \nabla\mathcal{F}^{-1}\left[\frac{\frac{\partial\tilde{\rho}}{\partial t}}{-k^2}\right], \qquad (6)$$

where $\tilde{\rho}$ is the Fourier transform of the PFC density field. This expression can be self-consistently determined during simulations. To avoid numerical divergence, we set the $k = 0$ component of $\vec{g}_l$ to 0. The longitudinal momentum can be interpreted as coming from shock fronts released or scattered from stress sources within the bulk polycrystal. Substituting Eq. (6) into Eq. (4) and Fourier transforming in time allows for an approximate measure of the longitudinal density of states, neglecting potential cross terms between $\vec{g}_l$ and $\vec{g}_s$. We expect these contributions to be quantitatively important but unnecessary to provide a qualitative picture of the phonon spectrum peaks.

The phonon density of states is intricate, with many frequency peaks closely distributed from one another. In a pristine lattice, Debye's theory of phonon dispersion predicts $\mathcal{G}(\omega) \propto \omega^{d-1}$, where d is the spatial dimension. Thus it is customary to report the ratio $\Gamma(\omega) = \frac{\mathcal{G}(\omega)}{\omega^{d-1}}$, which for a perfect crystal is expected to be constant. However, a realistic material will always exhibit some defect or metastable structures that modify the dispersion relation. As a consequence, additional peaks are found in $\Gamma(\omega)$, as illustrated in Fig. 3.

This is also observed in the terahertz frequency range where additional peaks are known to result. They are likely due to the dominance of mechanisms such as caging, scattering, and softening, although the precise cause of such peaks remains a subject of debate. Some peaks may be attributed to Van Hove singularities where the dispersion relation becomes singular [14]. Alternatively, the Ioffe-Regel limit may be the cause of maxima, wherein phonons with wavelengths less than their mean free path experience additional dampening [43]. Near 1.5 THz ($\omega \approx 22dt^{-1}$ in the PFC data of Fig. 3) a broad asymmetric peak called the boson peak has also been reported [12,13]. Originally documented in low-temperature glasses, the boson peaks is believed to occur due to excessive phonon softening [12,13,15] and has been found to occur in higher-temperature systems.

E. Variation of input kinetic energy

The phonon spectrum allows a description of the shock pulses that can be induced in a polycrystal during material processing. In reference to selective laser melting, depending on the energy imparted per area (fluence), recrystallization, plastic deformation, or fracture will ensue. Here electrons become excited, distributing their excitation energy to lattice vibrations on femto- to picosecond timescale [6]. Local energy densities may exceed various formation energies to allow for corresponding transformations. Alternatively, shock peening processes aim to increase dislocation density resulting from the interaction of the shock with material structure. Furthermore, in rolling, shock deep within the bulk is produced from the pressure imposed by the rollers. In the context of phase formations and phonon dampening, we view the energy imparted in these various processes as instantaneous, though we acknowledge that the early time behavior may play a dominant role.

We thus model the energy imparted onto a lattice as a kinetic energy, T_l, that can be related to the laser energy via $E_{\text{laser}} = \gamma T_l$. Here γ denotes an effective absorptivity of the crystal. This can be connected to the longitudinal momentum we determined earlier as

$$T_l(t) = \int_{\Omega} dr \frac{\langle \vec{g}_l(r,t) \cdot \vec{g}_l(r,t) \rangle}{2\rho_{\text{ref}}}, \tag{7}$$

where T is the effective temperature of the system and ρ_{ref} is the reference density.

As a first attempt to apply Eq. (7) to phase field crystal models, we introduce momentum through a normal distribution of the initial $\frac{\partial\rho}{\partial t}$ field, with average $\langle \frac{\partial\rho}{\partial t} \rangle_r = 0$ everywhere. For a given variance, 500 realizations of $\frac{\partial\rho}{\partial t}$ were constructed on a numerical grid the same size as our simulation domain in Table I (512×512). We subsequently found the momentum components, $\vec{g}_x$ and $\vec{g}_y$, to be approximately normally distributed. The inset of Fig. 4 illustrates the histogram of momenta, which when fitted and averaged over realizations provides a measure of the variance $\langle \vec{g_l} \cdot \vec{g_l} \rangle$. The main part of Fig. 4 plots the relation between input $\langle (\frac{\partial\rho}{\partial t})^2 \rangle$ and the measured $\langle \vec{g_l} \cdot \vec{g_l} \rangle$ for three domain sizes. For the 512×512 system, we find the linear relation $\langle \vec{g_l} \cdot \vec{g_l} \rangle = 1.267 \langle (\frac{\partial\rho}{\partial t})^2 \rangle$, with reduced $R^2 = 1.00$. Here the latter fit is applicable to the simulations that we report below. The above procedure provides a simple connection through Eq. (7) between $\langle (\frac{\partial\rho}{\partial t})^2 \rangle$ and the input kinetic energy.

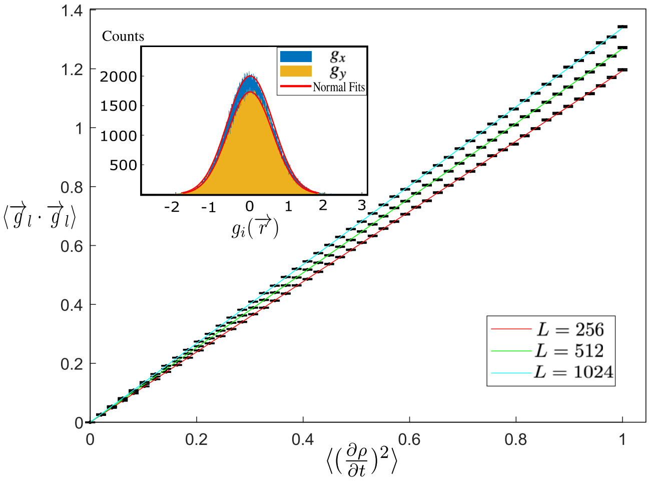

FIG. 4. Linear relationship obtained between $\langle \vec{g}_l \cdot \vec{g}_l \rangle$ and $\langle (\frac{\partial\rho}{\partial t})^2 \rangle$ for three different system sizes. The errorbars represent averaging over 500 realizations of the initial $\frac{\partial\rho}{\partial t}$. The inset shows the distribution of momenta for the case of $\langle (\frac{\partial\rho}{\partial t})^2 \rangle = 0.5$ ($\vec{g}_x$ and $\vec{g}_y$ are blue and orange, respectively).

III. INTERPRETATION OF RESULTS

A. Phonon relaxation mechanisms

Our phase field crystal simulations of polycrystal relaxation revealed a ubiquitous caging regime in the intermediate scattering function as seen in Fig. 2, that is, a multistage stretched exponential-like curvature. This interpretation is consistent with molecular dynamic simulations of Ni polycrystals, which found a similar two-timescale behavior [9]. This glassy caging behavior was lacking in simulations of an idealized crystal (without grain boundaries) as is illustrated in Fig. 2(b). Our results thus suggest that grain boundaries are the cause of the two-timescale behavior. Thus we suspect that increasing the defect density will result in materials that further resemble their metallic glass counterparts in regards to the phonon scattering spectrum. Our observations are mainly qualitative and would thus require a careful treatment of grain-boundary energy, such as in the work done by Mellenthin *et al.* [44] to connect to an quantitative material. We leave the study of how changing the polycrystal grain size and grain-boundary energy affect the phonon spectrum to future works.

In addition to the glassylike properties of polycrystals, we further observe that phonon scattering results in liquid pools that suppress further ballistic scattering and coarsen after formation. Some example videos of this process for different values of the dissipation constant (β_2) can be found in the Supplemental Material [45]. The liquid pools seem to result in ringing (boson peak) of the dynamic structure factor during the crossover from ballistic to diffusive motion. Here the density field has relaxed in the bulk grain, but has high activity near defects and grain boundaries. It is noted that in the limit of substantial low-wavelength dissipation, the ringing modes are suppressed as is shown in Fig. 2(b) when comparing the results for $\beta_2 = 1$ and $\beta_2 = 0.1$. Furthermore, the melt pool sizes are also found to be suppressed as β_2 was increased (see the Supplemental videos [45]). The pool nucleation mechanism is likely influenced by local grain energies, which is different for each polycrystalline sample studied. Here we have averaged over different grain-boundary energies; however, further analysis of the impact of grain-boundary energies may be conducted in future works. While the melt pools appear to form on grain boundaries, they can also form along slip planes of the host lattice structure when two grain boundaries are close to one another. These liquid pools recrystallize on longer timescales than their formation, potentially annealing into dislocations. It is noteworthy that the defected regions and recrystallization zones resemble the necklace structures found in dynamic recrystallization experiments [46] that can lead to serrated grain boundaries. Importantly, energy is being added to the system by external mechanical deformation. The induced strain subsequently generates phonons propagating through the lattice and carry the energy to the grain boundaries. Typically, when a material is externally strained, recrystallization takes place on the grain boundary within the bulk. When the recrystallized grains are small relative to their host, the morphology resembles a necklace. As the input energy is increased, further heterogeneous nucleation takes place. In certain scenarios, the liquid pools could become highly depleted in density, where we suspect cavitation or fracture would commence. Additionally, we note in multicomponent alloys, the high energetics may induce concomitant precipitation similar to the work by Medina *et al.* where energy is added through external strain loading [47]. These aforementioned processes thus describe a recrystallization mechanism occurring as a result of phonon caging and scattering.

Further analysis of the phonon scattering spectrum through the longitudinal phonon density of states revealed the emergence of resonance peaks. We note that the negative density of states should be viewed as a depletion of available sites, since we are only considering longitudinal components of the velocity. In Fig. 3 we show the longitudinal density of states averaged over 10 polycrystals for two values of β_2 that control the low-wavelength phonon dissipation. In both cases, we see a peak at roughly $\omega \approx 22\ dt^{-1}$. An inset is provided expanding this region. In the case of the lower dissipation (orange), we find additional peaks at lower frequencies. In the latter case, phonons propagate further between potential sites of scattering and softening. To this extent, we believe the additional resonances are caused by the phonon scattering or softening at boundaries. This interpretation is consistent with dispersion relation calculations that suggest softening as a culprit for low-frequency peaks. Meanwhile, we suspect the high-frequency peak could be a potential boson peak. We note, however, that this peak may be an artifact of the approximations that went into deriving Eq. (4). As result, further metrics to connect the high-frequency peak may be necessary. In particular, low-frequency shear waves may interact with the longitudinal modes. Importantly, the features of the resonance peaks are qualitatively consistent with experimental measurements of laser irradiated thin films, which are measuring the process at much shorted timescales [48,49]. Waldecker *et al.* further highlight the dominant activity of the longitudinal acoustic modes, such as those we have been able to measure [49]. More intricate hydrodynamic amplitude variants of the phase field crystal model that explicitly track the velocity vector field may also be able to elucidate the shear contributions.

B. Laser melting

Our discussion thus far has dealt with polycrystalline lattices subjected to large thermal noise. These investigations are thus applicable to thermal annealing experiments. However, in the rapid solidification encountered in processes such as additive manufacturing, energy is transferred near instantaneously from a shock. Following the procedure described in the previous section, we add an initial burst of kinetic energy, E_o, in the form of a density distribution corresponding to an initial $\langle (\frac{\partial \rho}{\partial t})^2 \rangle$. This addition represents the first attempt at describing the energy embedded in shock fronts that are found in both bulk material that are subjected to mechanical deformation [46] and in laser melting systems [50]. Subsequently, we compare the defect fraction (in accordance with the thresholding method described in Appendix B) over 10 simulations of different realizations of a fixed input energy. Additionally, our simulations were repeated over different polycrystalline configurations. The defect fraction composed of structural defects, such as dislocations and melt pools. The simulation is supplemented with a small noise, $\sigma = 0.01$, which accounts for rapid dynamics below the coarse-graining scale of the PFC model. Figure 5 illustrates that an increasing input energy leads to an increasing maximal defect fraction, as measured using the procedure in Appendix B. Figure 5(a) demonstrates the tracked defect fraction as a function of time for different input energies. Figures 5(c_1)–5(c_4) show the typical density fields at $t = 1500\Delta t$ for different input kinetic energies, with the insets showing the defect fraction thresholding. Figure 5(b) highlights the maximally achieved defect fraction as a function of the input energy. It is noted that the defect fraction shown in the density maps as insets in Fig. 5. This metric subsumes features such as grain boundaries, dislocations, and metastable liquid zones, all of which are created due to the stress or strain imparted by the input laser energy. We observe that these all serve as templates from which subsequent recrystallization occurs in the sample. In that sense, we are seeing both traditional mechanisms of recrystallization caused by stress or strain in the solid state [3] but also predicting, as far as we know, novel mechanisms such as local recrystallization arising from metastable liquid or amorphous pools. Such mechanisms are expected to be ubiquitous in shocked materials, excited by laser irradiations [50,51].

In analogy to the metastable Ostwald ripening curves [52], we attempt to describe defect nucleation rate through rate relation considerations. In this scenario, the energy dissipates roughly exponentially in time, $E_{\rm in}(t) \approx E_o e^{-bt}$, with b dependent on the dampening in Eq. (2). Once an energy threshold has been reached, melt pools are found to form at defect sites and along slip lines of the crystal in relation to our earlier

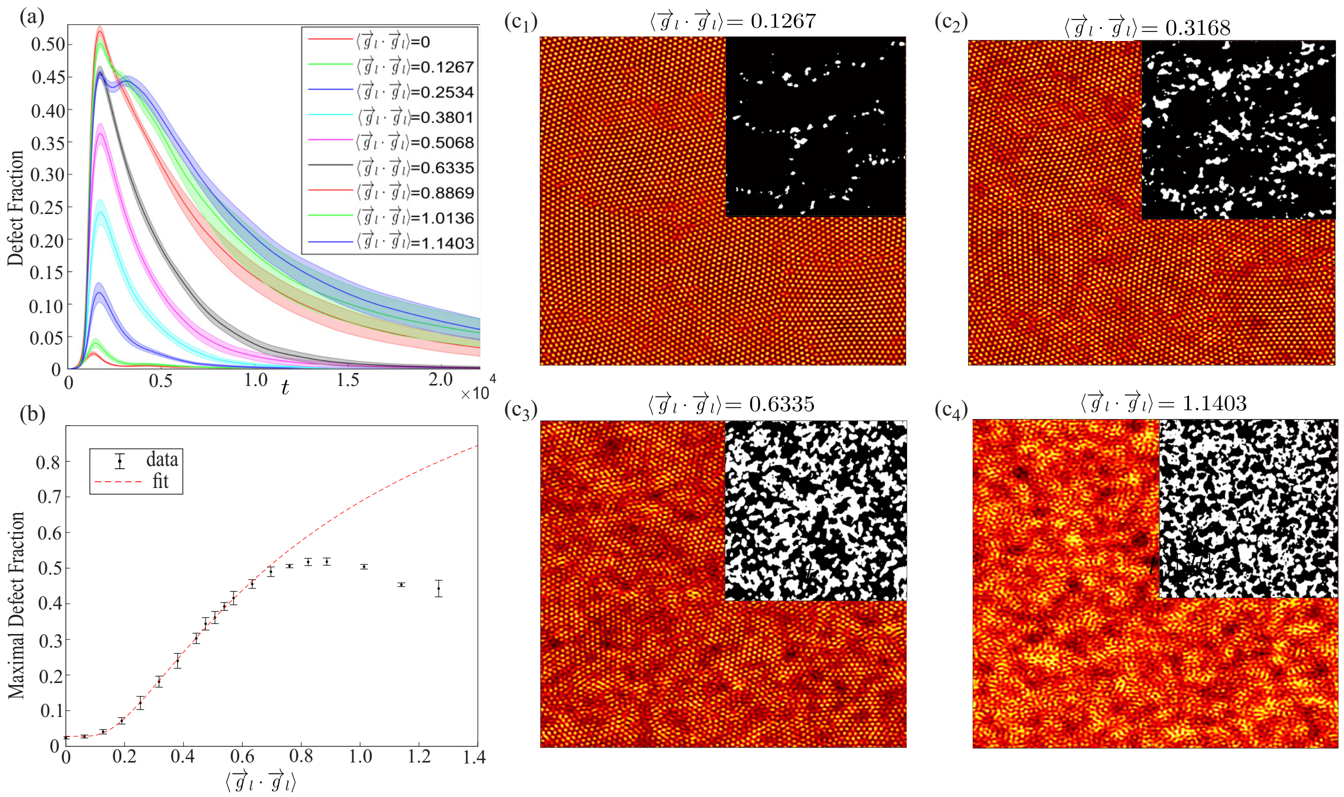

FIG. 5. This figure highlights the response of a crystal to an initial input of kinetic energy. (a) The defect fraction measured as a function of time for different input energies. The associated error bars are captured by transparent borders denoting the standard error, when averaged over different polycrystal samples. (b) The maximal achieved defect fraction as a function of the input energy. Thereto we fit Eq. (8) (red line) with adjusted $R^2 = 0.9985$. Here $a_1 = 10.46$, $a_2 = 0.1051$, $a_3 = 0.6092$, and $a_4 = -10.44$. Error bars denote the standard error measured over different polycrystal samples. (c$_1$)–(c$_4$) The density field at time $1500\Delta t$ for different input kinetic energies for the same sample. The insets represent a thresholding analysis to determine the defect fraction.

results. This qualitative morphology is in further corroboration with the necklace structures described above, We argue that the liquid pools have a substantial amount of energy buried in their solid-liquid interfaces. Thus we make the approximation that the volume of a given melt pool is proportional to boundary energy. We thus make the conjecture,

$$\frac{\partial E_{\text{boundary}}}{\partial t} = \Gamma_+ - \Gamma_- = e^{-\frac{E_A}{E_o e^{-bt}}} E_{\text{boundary}} - \Gamma_{\text{Thermodynamic}}, \qquad (8)$$

where $\Gamma_+ = e^{-\frac{E_A}{E_{\text{in}}}} E_{\text{boundary}}$ represents the energy absorption rate expected to occur uniformly across the boundary. Here E_A denotes an effective activation energy for melt-pool growth. As a result of the metastability of the melt pools, a thermodynamic restoring force that disperses interfaces is introduced through Γ_-, which is taken here as a constant. Equation (8) can be solved in the limit of $b \ll 1$ to yield,

$$E_{\text{boundary}}(t) \approx C_1 e^{t e^{-\frac{E_A}{E_{\text{in}}}}} + \Gamma_{\text{Thermodynamic}} e^{\frac{E_A}{E_{\text{in}}}}. \qquad (9)$$

The integration factor C_1 includes an energy dependence that needs be determined. We then determine the time, $t_{\max}$, at which the boundary energy is maximized. This is achieved by setting Eq. (8) to zero and performing a Taylor expansion of Eq. (8) for small t. Recasting the Eq. (9) results in the approximate form,

$$E_{\text{boundary}}(t_{\max}, E_o) \approx a_1 e^{a_2 e^{-\frac{a_3}{E_o}}} + a_4. \qquad (10)$$

Here a_i are the coefficients of our kinetic theory. Note that a_3 has dimensions of energy and may be viewed as an effective activation energy to form metastable structures. The relation is expected to be independent of spatial dimension. However, we expect the boundary absorptivity to deviate as a result of the dislocation dimensionality. We have only aim here to describe the maximally achieved defect fraction subjected to an energy burst in the sample. To further account for healing and coarsening, $\Gamma_{\text{Thermodynamics}}$ may be extended to include energy and time dependence. We leave such a study for future work. We also note that equation (10) only accounts for a single phase transformation. In multiphase studies (e.g., precipitation and void) Eq. (8) may be supplemented by additional activation-energy terms.

We fit Eq. (10) to the maximal defect fraction extracted from the data of Fig. 5(a). The results are shown in Fig. 5(b). The results suggest are consistent with the above analytical theory for low input energies. It is noted that Eq. (8) represents a rather crude approximation of the system, since grain-boundary structure, density segregation, fracture nucleation, and temperature effects can also impact the resultant curve. In particular, our analytical theory poorly predicts the high-energy regime where a secondary defect peak is found to emerge in the simulation data of Fig. 5(a), which we believe is a result of the thresholding used to determine the defect fraction. In particular, this is because the high-energy density fields [Fig. 5(c_4)] are found to be highly amorphous and not accounted for by the thresholding. We note that phase field crystal models may breakdown at this high-energy limit as other structures such as metallic glass or fracture may form. To this end, future work may extend our study to multicomponent materials following Ofori *et al.* [20]. Alternatively, fracture may be treated through the introduction of a vapor phase as in the work of Frick *et al.* [37]. We expect that the trends reported here are expected to be true independent of spatial dimension. However, a more quantitative validation of our results with experiments may also require the inclusion of latent heat to extend the theory to account for consistent coarsening timescales. Nonetheless, we have illustrated in this work that laser-induced recrystallization should include a pathway involving heterogeneous nucleation from nanoliquid pools found at high-energy grain boundaries.

IV. SUMMARY

In this article we have used PFC modeling with two-timescale dynamics to examine phonon excitation in polycrysatlline nanomaterials. In particular, we have investigated the dynamic structure factor of a polycrystalline material subjected to multitimescale dynamics. In comparison to the single exponential decay of an idealized lattice, polycrystals are found to exhibit a two-step decay process, commonly exhibited by glasses. A caging regime is found that results from phonon softening and is affected by the amount of high-wavelength dissipation. Phonon accumulation was also found to result in the formation of metastable melt pools. We have also performed the first analysis of the longitudinal phonon density of states with phase field crystal models. Herein we uncovered multiple peaks that emerge from phonon scattering and a broad peak, which is potentially relatable to the boson peak. As we have described, a more detailed investigation of the phonon scattering properties may be explored through use of hydrodynamic coupled phase field crystal models that explicitly evolve a velocity field.

Our phonon relaxation studies were then used to investigate the rapid transfer of energy into polycrystalline materials and their subsequent relaxation and recrystallization. We found that increasing input energy resulted in an increase of the defect density and the formation of liquid pools. We developed a simple theory to describe the maximally achieved defect fraction as a function of input energy. At low energies our results are in a agreement with the theory. Thus our work suggests that early stage shock-induced recrystallization is dominated by the formation of melt pools. Future experimental work may be performed to assess the validity of our theory. Owing to the density depleted pools, high input energies are further expected to cause cavitation and fracture or nucleation of other metastable structures. Such processes may be the topics of future studies with the use of multicomponent models or vapor phase models.

ACKNOWLEDGMENTS

We thank Prof. Bradley Siwick for stimulating discussions. We thank Natural Sciences and Engineering Research Council of Canada and *le Fonds de recherche du Quebec-Nature et technologies* for funding support. Additionally, we thank Calcul Québec and the Digital Research Alliance of Canada for computing resources.

APPENDIX A: PHASE DIAGRAM

The phase field crystal model is built as an expansion of the free energy about the liquidus for the study of solidification. For the details, we refer the reader to the work of Provatas *et al.* [35]. Here an effective temperature is varied through the parameters B_l or B_x that enter into Eq. (1). To understand the preferential selection of crystalline order versus uniform liquid state, it is customary to make a one-mode expansion of the density,

$$\rho(r) = \overline{\rho} + \Sigma_{G_j} A_{|G_j|} e^{iG_j\cdot r}. \tag{A1}$$

The parameter $\overline{\rho}$ represents the uniform average density adopted by the liquid phase. A_{G_j} are the amplitudes centered about the reciprocal lattice vectors G_j, which act as order parameters of the crystal's translational symmetry. Substitution of Eq. (A1) into (1) and subsequent integration over a unit cell represents the approximate bulk free energy. All further free parameters, such as A_{G_j} and R, would need to be minimized, the solutions of which enumerate the bulk free energies of the thermodynamic phases. We emphasize that this expansion is an ansatz of the minimal energy states, which in generality should be verified through numeric simulation.

One may then solve the condition of phase coexistence:

$$\mu_1 = \mu_2, \tag{A2a}$$

$$\overline{\rho_1}\mu_1 = \overline{\rho_2}\mu_2. \tag{A2b}$$

Here $\mu_i = \frac{\delta F}{\delta \rho}$ is the chemical potential and $\overline{\rho_i}$ coexistence density associated to phase i. Although explicit calculation of the above relations is possible, one can also make use of

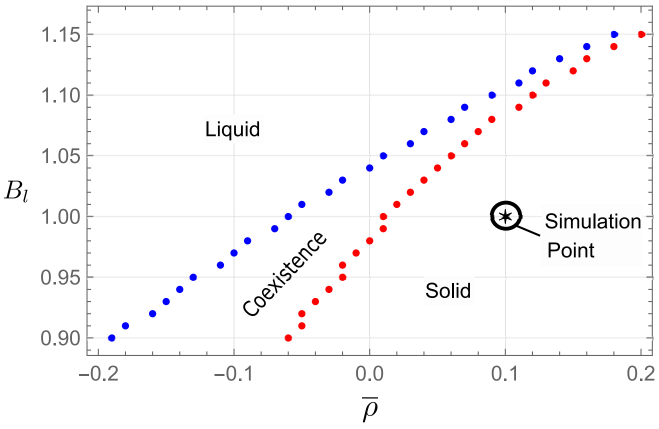

FIG. 6. This figure illustrates the phase diagram obtained through a one-mode ansatz of the equilibrium crystal structure. The corresponding stable phase region is as denoted. The star denotes the phase state used for our study.

a convex hull algorithm of the free energy as detailed by Seymour *et al.* in their thesis [53]. Repeating the calculation at different temperatures results in a phase diagram as illustrated in Fig. 6. The highlighted points denote the temperatures and density used throughout this paper.

APPENDIX B: IMAGING METHODS

The density field carries large amounts of information in the Fourier modes. One can analyze the deviations from the mode expansion form of Eq. (A1) to extract specific information about interface structures. As introduced in earlier work, the strain field can be extracted from

$$\nabla \cdot u \approx \mathcal{F}^{-1}\left[k \exp -\frac{k^2}{\sigma_0}\mathcal{F}\left[\rho\mathcal{F}^{-1}\left[(k-|G|) \times \exp \frac{-(k-|G|)^2}{\sigma_0}\mathcal{F}[\rho]\right]\right]\right], \tag{B1}$$

where $\mathcal{F}$ denotes the Fourier transform operator. We use this filter not only for visualization of dislocations but also as a metric for the dislocation density of a given polycrystal. The inset of Fig. 1 shows and example of this filter.

We also make use of

$$\mathcal{F}^{-1}\left[e^{-\frac{k^2}{\sigma_0}}\mathcal{F}[|\rho|]\right] \approx \overline{\rho}^2 + |A_G|^2, \tag{B2}$$

which combined with thresholding allows for a rough characterization of the local phase. Our studies of defect fraction utilized a $\sigma_0 = 0.3$. The thresholding entailed summing the number of pixels with density values above 0.3 and subsequent division by the total pixel number. To our knowledge, this type of approach was first described by Kocher *et al.* [54], when attempting to coarse-grain the phase field crystal model to a single order parameter.

APPENDIX C: FINITE-SIZE ANALYSIS

Since our simulations are performed on a two-dimensional periodic domain, wave attenuation needs to be ensured to occur on scales larger than the system size. To ensure that peaks detected with the density of states were not artifacts of finite-size effects, we performed additional simulations on numerical grids with lengths 256 and 1024 grid points. We refer the reader to the Supplemental Material for videos of the process [45]. We found that the system size had negligible affect on the melting and recrystallization behavior described throughout this work or on the presence of phonon softening that resulted in two-timescale dynamics.

---

[1] F. Humphreys and M. Hatherly, in *Recrystallization and Related Annealing Phenomena*, 2nd ed., edited by F. Humphreys and M. Hatherly (Elsevier, Oxford, 2004), pp. 91–119.

[2] C. M. Sellars and J. A. Whiteman, Met. Sci. **13**, 187 (1979).

[3] S. Gao, Z. Hu, M. Duchamp, P. S. R. Krishnan, S. Tekumalla, X. Song, and M. Seita, Acta Mater. **200**, 366 (2020).

[4] F. C. Pinto, L. Aota, I. Souza Filho, D. Raabe, and H. R. Z. Sandim, J. Mater. Sci. **57**, 9576 (2022).

[5] U. Andrade, M. Meyers, K. Vecchio, and A. Chokshi, Acta Metall. Mater. **42**, 3183 (1994).

[6] B. J. Siwick, J. R. Dwyer, R. E. Jordan, and R. J. D. Miller, Science **302**, 1382 (2003).

[7] M. I. Arefev, M. V. Shugaev, and L. V. Zhigilei, Sci. Adv. **8**, eabo2621 (2022).

[8] F. Demmel, Phys. Rev. B **101**, 014207 (2020).

[9] H. Zhang, D. J. Srolovitz, J. F. Douglas, and J. A. Warren, Proc. Natl. Acad. Sci. USA **106**, 7735 (2009).

[10] D. G. Cahill, W. K. Ford, K. E. Goodson, G. D. Mahan, A. Majumdar, H. J. Maris, R. Merlin, and S. R. Phillpot, J. Appl. Phys. **93**, 793 (2003).

[11] B. Golding and J. E. Graebner, Echo phenomena in disordered solids, in *Phonon Scattering in Condensed Matter*, edited by H. J. Maris (Springer US, Boston, MA, 1980), pp. 11–20.

[12] S. Ren, H.-X. Zong, X.-F. Tao, Y.-H. Sun, B.-A. Sun, D.-Z. Xue, X.-D. Ding, and W.-H. Wang, Nat. Commun. **12**, 5755 (2021).

[13] M. González-Jiménez, T. Barnard, B. A. Russell, N. V. Tukachev, U. Javornik, L.-A. Hayes, A. J. Farrell, S. Guinane, H. M. Senn, A. J. Smith, M. Wilding, G. Mali, M. Nakano, Y. Miyazaki, P. McMillan, G. C. Sosso, and K. Wynne, Nat. Commun. **14**, 215 (2023).

[14] S. N. Taraskin, Y. L. Loh, G. Natarajan, and S. R. Elliott, Phys. Rev. Lett. **86**, 1255 (2001).

[15] M. Baggioli and A. Zaccone, Phys. Rev. Res. **2**, 013267 (2020).

[16] A. Zaccone and M. Baggioli, Phys. Rev. Res. **4**, 029001(E) (2022).

[17] K. R. Elder and M. Grant, Phys. Rev. E **70**, 051605 (2004).

[18] K. R. Elder, N. Provatas, J. Berry, P. Stefanovic, and M. Grant, Phys. Rev. B **75**, 064107 (2007).

[19] M. Greenwood, N. Provatas, and J. Rottler, Phys. Rev. Lett. **105**, 045702 (2010).

[20] N. Ofori-Opoku, V. Fallah, M. Greenwood, S. Esmaeili, and N. Provatas, Phys. Rev. B **87**, 134105 (2013).

[21] Z.-L. Wang, Z. Liu, W. Duan, and Z.-F. Huang, Phys. Rev. E **105**, 044802 (2022).

[22] J. Berry, K. R. Elder, and M. Grant, Phys. Rev. B **77**, 224114 (2008).

[23] J. Berry and M. Grant, Phys. Rev. Lett. **106**, 175702 (2011).

[24] J. Berry, N. Provatas, J. Rottler, and C. W. Sinclair, Phys. Rev. B **86**, 224112 (2012).

[25] P. Stefanovic, M. Haataja, and N. Provatas, Phys. Rev. E **80**, 046107 (2009).

[26] V. Skogvoll, M. Salvalaglio, and L. Angheluta, Modelling Simul. Mater. Sci. Eng. **30**, 084002 (2022).

[27] P. Stefanovic, M. Haataja, and N. Provatas, Phys. Rev. Lett. **96**, 225504 (2006).

[28] S. Majaniemi and M. Grant, Phys. Rev. B **75**, 054301 (2007).

[29] D. Burns, N. Provatas, and M. Grant, Modelling Simul. Mater. Sci. Eng. **30**, 064001 (2022).

[30] J. Berry and M. Grant, Phys. Rev. E **89**, 062303 (2014).

[31] Z. Chen, Z. Wang, X. Gu, Y. Chen, L. Hao, J. de Wit, and K. Jin, Appl. Phys. A **124**, 385 (2018).

[32] S. Abdalla, A. J. Archer, L. Gránásy, and G. I. Tóth, J. Chem. Phys. **157**, 164502 (2022).

[33] M. Vasin and V. Ankudinov, Math. Meth. Appl. Sci. 9207 (2023).

[34] Y. Singh, Phys. Rep. **207**, 351 (1991).

[35] N. Provatas and K. Elder, Phase field crystal modeling of pure materials, in *Phase-Field Methods in Materials Science and Engineering* (John Wiley & Sons, New York, 2010), Chap. 8, pp. 167–208.

[36] G. Kocher and N. Provatas, Phys. Rev. Lett. **114**, 155501 (2015).

[37] M. J. Frick, E. Wilson, and N. Provatas, Phys. Rev. Mater. **7**, 023405 (2023).

[38] K. Wang, S. Xiao, J. Chen, S. Yao, W. Hu, W. Zhu, P. Wang, and F. Gao, Int. J. Plast. **157**, 103386 (2022).

[39] M. Hillert, M. Schwind, and M. Selleby, Acta Mater. **50**, 3285 (2002).

[40] T. Pinomaa, M. Lindroos, P. Jreidini, M. Haapalehto, K. Ammar, L. Wang, S. Forest, N. Provatas, and A. Laukkanen, Philos. Trans. R. Soc. A **380**, 20200319 (2022).

[41] C. A. Angell, K. L. Ngai, G. B. McKenna, P. F. McMillan, and S. W. Martin, J. Appl. Phys. **88**, 3113 (2000).

[42] S. L. Seyler and C. E. Seyler, J. Chem. Phys. **159**, 054108 (2023).

[43] Y. M. Beltukov, C. Fusco, D. A. Parshin, and A. Tanguy, Phys. Rev. E **93**, 023006 (2016).

[44] J. Mellenthin, A. Karma, and M. Plapp, Phys. Rev. B **78**, 184110 (2008).

[45] See Supplemental Material at http://link.aps.org/supplemental/10.1103/PhysRevMaterials.7.083402 for aset of simulation movies.

[46] D. Ponge and G. Gottstein, Acta Mater. **46**, 69 (1998).

[47] S. F. Medina, J. Mater. Sci. **32**, 1487 (1997).

[48] L. Waldecker, R. Bertoni, and R. Ernstorfer, J. Appl. Phys. **117**, 044903 (2015).

[49] L. Waldecker, R. Bertoni, R. Ernstorfer, and J. Vorberger, Phys. Rev. X **6**, 021003 (2016).

[50] M. M. Budzevich, V. V. Zhakhovsky, C. T. White, and I. I. Oleynik, Phys. Rev. Lett. **109**, 125505 (2012).

[51] V. Zhakhovsky, Y. Kolobov, S. Ashitkov, N. Inogamov, I. Nelasov, S. Manokhin, V. Khokhlov, D. Ilnitsky, Y. Petrov, A. Ovchinnikov, O. Chefonov, and D. Sitnikov, arXiv:2306.09100.

[52] C. Sagui, D. S. O'Gorman, and M. Grant, Phys. Rev. E **56**, R21 (1997).

[53] M. Seymour, Study of multi-point interactions in PFC modelsfor complex structural transformations, Ph.D. thesis, McGill University, Canada, 2018.

[54] G. Kocher and N. Provatas, Phys. Rev. Mater. **3**, 053804 (2019).